Mon. Not. R. Astron. Soc. **000**, 000–000 (0000) Printed 26 January 2011 (MN LATEX style file v2.2)

An atlas of mid-infrared spectra of star-forming and active galaxies

A. Hernán-Caballero[1,2⋆] and E. Hatziminaoglou[3]
[1]*Instituto de Estructura de la Materia, Consejos Superior de Investigaciones Cientficas, Serrano 121, 38006 Madrid, Spain*
[2]*Centro de Astrobiología (CSIC/INTA), Ctra. de Torrejón a Ajalvir km 4, 28850 Torrejón de Ardoz, Spain*
[3]*European Southern Observatory, Karl-Schwarzschild-Str. 2, 85748 Garching bei München, Germany*

arXiv:1101.4794v1 [astro-ph.CO] 25 Jan 2011

Accepted ..... Received .....;

ABSTRACT

We present a panoramic atlas of *Spitzer*/IRS spectra of extragalactic sources collected from the recent literature, with value added measurements of their spectral features obtained in a homogeneous and concise manner. The atlas covers the full spectrum of the extragalactic universe and includes star forming galaxies, obscured and unobscured active galaxies, luminous and ultra-luminous infrared galaxies, and hybrid objects. Measured features such as the polycyclic aromatic hydrocarbons, the strength of the silicates in emission or absorption around 9.7 μm, rest-frame monochromatic luminosities or colours, combined with measurements derived from spectral decomposition, are used to establish diagnostics that allow for classification of sources, based on their infrared properties alone. Average templates of the various classes are also derived. The full atlas with the value added measurements and ancillary archival data are publicly available at http://www.denebola.org/atlas, with full references to the original data.

Key words: galaxies: high-redshift – galaxies: active – galaxies: starburst – infrared: general – infrared:galaxies – quasars: general

1 INTRODUCTION

The mid-to-far infrared spectral range holds the key to the physical processes that shape the life and properties of galaxies, namely star formation and nuclear activity. This spectral domain, and with the exception of the very bright emission lines of the brightest sources, was almost unaccessible from the ground and until 15 years ago, when the sensitivity and large wavelength coverage of the Infrared Space Observatory (ISO) allowed the detailed study of large numbers of nearby starburst galaxies and active galactic nuclei (AGN) and lead to the first mid-infrared (MIR) diagnostic tools. ISO studies observed, among other things, the presence of polycyclic aromatic hydrocarbon (PAH) features in the majority of star-forming galaxies (Lutz et al. 1998; Rigopoulou et al. 1999) and their more scarce appearance in AGN (e.g. Sturm et al. 2000), as well as the presence of a silicate feature in absorption in type 2 AGN (Clavel et al. 2000).

Though the studies carried out with ISO brought a break through in our understanding of star formation in galaxies, it was the *Spitzer* Space Telescope with its MIR cameras IRAC and MIPS, and the InfraRed Spectrograph (IRS) that revolutionised our knowledge on the starburst and AGN phenomena and their connection. IRAC broad band MIR photometry alone allowed for a rough classification among AGN and a distinction between active and star-forming galaxies (e.g. Lacy et al. 2004; Stern et al. 2005; Hatziminaoglou et al. 2005, 2009), while IRS observations of hundreds of extragalactic sources provided with more elaborate diagnostic tools (e.g. Spoon et al. 2007) and showed that their MIR spectra are richer and more complex than once assumed. The new discoveries, however, raised new issues that models are now challenged to reproduce. The silicate emission feature in type 1 AGN peaks at longer wavelengths than the 9.7 μm predicted by the models (e.g. Siebenmorgen et al. 2005; Hao et al. 2005); silicate emission has also been observed in type 2 AGN (Sturm et al. 2006; Teplitz et al. 2006; Nikutta et al. 2009) in apparent contradiction to at least some of the suggested dust geometries; and PAH emission is present in many quasars (e.g. Schweitzer et al. 2006), despite previous theories postulating their destruction in the vicinity of the active nucleus. Meanwhile, accurate measurements of PAH features in star-forming galaxies are made difficult by the presence of other features, such as the deep silicate absorption at 9.7 μm or an underlying AGN continuum.

Understanding the processes linking different galaxy populations and finding their distinctive characteristics requires the comparison of the properties of large samples, selected with different but well understood criteria. Studies of individual samples usually pursue specific goals, and basic MIR properties for diagnostics (such as the strength of the silicate features and PAH bands) are measured in ways adapted to the needs of each individual study, but

⋆ e-mail: ahc@denebola.org

not necessarily consistently across samples, making a direct comparison of results painful, if not impossible.

With this in mind, we compiled a list of 739 *Spitzer*/IRS spectra of extragalactic sources, the largest of its kind to date, previously scattered in the recent literature. The sample, though not statistical, comprises a variety of objects, namely type 1, 2 and intermediate AGN, ULIRGs, starburst and sub-mm galaxies, with a large span of spectral properties such as PAH and silicate features, continua and distinct physical characteristics. The MIR properties were meassured in a concise way for all objects and can thus be directly compared. The paper is structured as follows. §2 describes the sample selection, overall properties and collection of ancillary data; §3 presents the extraction of the IRS spectra and calibration procedure followed; sections 4 and 5 detail the methods used to measure MIR spectral properties and the composite spectra obtained for the various subsamples, respectively; §6 reproduces a few common diagnostic diagrams and finally §7 summarizes our conclusions.

The full collection of IRS spectra with references to the original data, ancillary data and additional measurements are available at http://www.denebola.org/atlas.

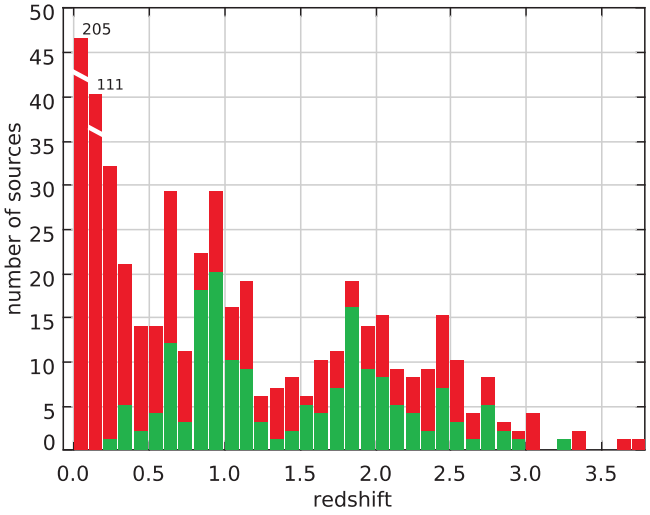

Figure 1. Redshift histogram for the 695 sources with spectroscopic redshifts in the sample. The red bars indicate optical redshifts, while the green bars represent the MIR ones. Bars for the first two redshift bins are truncated to improve readability.

2 SAMPLE SELECTION

The sample hereby presented is drawn from papers in the literature presenting *Spitzer*/IRS spectroscopy of active and star-forming galaxies, and contains a wide variety of targets including Starbursts, Seyferts, LINERs, ULIRGs, QSOs, SMGs and radio galaxies, among others. A total 739 unique sources are selected from Brand et al. (2008), Brandl et al. (2006), Buchanan et al. (2006), Cao et al. (2008), Dasyra et al. (2009), Deo et al. (2007), Farrah et al. (2009), Haas et al. (2005), Hao et al. (2005), Hernán-Caballero et al. (2009), Hiner et al. (2009), Imanishi et al. (2007, 2010), Imanishi (2009), Lacy et al. (2007), Leipski et al. (2009), Lutz et al. (2008), Maiolino et al. (2007), Menéndez-Delmestre et al. (2009), Murphy et al. (2009), Netzer et al. (2007), Polletta et al. (2008), Pope et al. (2008), Shi et al. (2006), Siebenmorgen et al. (2005), Sturm et al. (2005, 2006), Tommasin et al. (2008), Valiante et al. (2007), Weedman et al. (2005, 2006a,b, 2009), Willett et al. (2010), Wu et al. (2009), Yan et al. (2007) and Zakamska et al. (2008).

Table 1 summarizes the type and number of spectra and observation mode for each subsample. For a more detailed description of the selection criteria and properties of the individual subsamples we defer the reader to the corresponding papers.

Spitzer/IRS data for sources in the sample include observations with both the Low-Resolution (R∼100) and High-Resolution (R∼600) IRS modules, all performed in staring-mode, except for the sources from Buchanan et al. (2006) and Wu et al. (2009), where observations were performed in spectral mapping mode, but only the spectrum obtained with the slit placed in the galactic nucleus is given. Maximum spectral coverage is 5-38μm in the Low-Res module and 10-35μm in the High-Res one, but in many faint targets only a subset of Low-Res modules is applied, resulting in a reduced spectral coverage that is not uniform even within the same subsample.

Sources at intermediate and high redshift appear unresolved to the IRS, and thus the spectra integrate the emission of the whole galaxy. By contrast, in nearby targets the spectra only sample the nuclear region. Our selection does not put constraints on redshift, not even the existence of a consistent redshift estimate, but individual subsamples usually target certain redshift range, or indirectly bias the selection through flux or colour constraints.

Spectroscopic redshifts (either from optical or MIR spectroscopy) are available for 695 of the 739 sources. Redshifts are obtained from the literature and cross-checked with the NASA Extragalactic Database (NED). 525 redshifts come from optical spectra, while 170 sources (mostly obscured high-*z* targets) rely on a redshift estimate from their IRS spectrum. In targets where both optical and MIR spectroscopic redshifts are available, priority is given to the former, except in cases of strong discrepancy in which the optical redshift is flagged as unreliable or the MIR spectrum shows very clear PAH bands. The remaining 44 sources have no published spectroscopic redshift, or it is uncertain. They are not removed from the sample, but will be ignored in the subsequent analysis.

About half of the sample, 347 sources, have redshifts below z=0.3, while the rest spans a large redshift range up to z∼3.7 (Figure 1). Spectral coverage in rest frame wavelength is in all cases within 1.2 and 38 μm, with 389 sources sampling the 5.5-14 μm range in its entirety and 550 the critical 8-12μm range, which contains both the 10 μm silicate feature and 11.3 μm PAH band (see Figure 2).

An optical spectroscopic classification is also available for most sources. A positional match with the 13th version of the Veron Catalogue of Quasars & AGN (VERONCAT; Veron & Veron 2006) yields 361 matches; for these sources, we adopt the activity type designation in the VERONCAT. For the remaining ones we adopt the optical classification in NED, when available, or at the very least a broad class (e.g.: ULIRG, SMG) either from NED or the individual papers the spectra are taken from. Some sources are put in more than one classes. For example, a starburst galaxy with a Seyfert 2 nucleus will retain both starburst and Seyfert 2 clasifications.

To deal with the large variety of spectral types, we group them into 10 categories, namely: Seyfert 1 (Sy1), Seyfert 2 (Sy2), intermediate Seyfert type (Sy1.X), LINER, Quasar (QSO), type 2 Quasar (QSO2), Starburst, ULIRG, SMG and “other” when none of the above classifications apply.

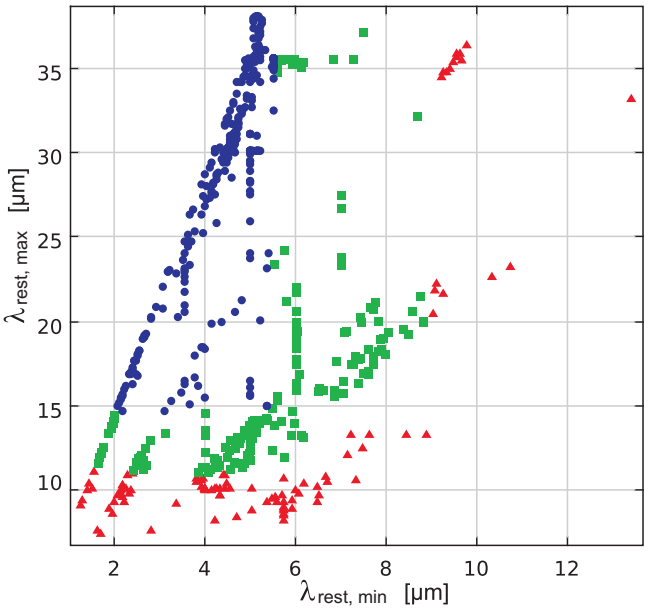

Figure 2. Restframe wavelength coverage for the 695 sources with spectroscopic redshift in the sample. Each point represents one source, with the X and Y coordinates indicating the shortest and longest wavelengths sampled in the IRS spectrum, respectively. Symbols indicate spectral coverage in the 5–15μm restframe range: >95% (blue circles), between 60% and 95% (green boxes) and <60% (red triangles).

We set a threshold value of $\nu L_\nu(7\mu m) = 10^{44}$ erg s^{-1} (roughly the output of the least luminous ULIRG of this sample), above which all type 1 and type 2 AGN are considered as QSO or QSO2, while keeping the Seyfert 1 and Seyfert 2 designations for the lower luminosity Seyferts. The LINER class does not include LINER cores of ultraluminous and starburst galaxies, as their MIR spectrum is typically dominated by the host galaxy.

3 EXTRACTION OF THE SPECTRA

To obtain the IRS spectra we have not gone through the normal process of querying the *Spitzer* archive, reduce the raw Spitzer/IRS data and extract the spectra. Instead, we have relied on Postscript figures contained in papers submitted to the arxiv.org preprint archive. This approach has several shortcomings that we describe later, and is not optimal for a detailed analysis of individual targets. Nevertheless, it provides a cost-efficient means for performing statistical studies on the largest starburst and active galaxy sample compiled to date.

Sets of points representing the spectra in the figures are transformed from Postscript coordinates to wavelength and flux values using software developed by the authors. Paper figures represent the spectra in many different fashions: the independent variable is usually wavelength, whether in the observed or rest frame, but it can also be frequency. For the dependent variable there are several values of choice: f_ν, f_λ, νf_ν, νL_ν, etc., that in addition are expressed in different units systems and plotted in linear or logarithmic scale.

To homogenize the sample, we convert all spectra back to the same units provided by the *Spitzer* IRS reduction pipeline: observed wavelength in micron and spectral flux density in Jy. The accuracy with which the original wavelength and flux values are recovered is limited by the resolution of the Postscript figure; nevertheless, the uncertainty that this introduces to the wavelength calibration is about an order of magnitude smaller than the spectral resolution (R∼100) in the Low-Resolution module of IRS, and thus its impact is negligible.

Since the uncertainties in the flux density of the spectra are not shown in most of the figures, we devised a procedure to estimate them based on individual exposure times, obtained from queries to the *Spitzer* archive when they were not indicated in the corresponding papers, using the SPEC-PET exposure time calculator. Flux uncertainties estimated by SPEC-PET are corrected for wavelength sampling (SPEC-PET assumes R=50), with an additional $\sqrt{2}$ factor to account for the noise introduced by standard background subtraction. We use two different methods to evaluate the accuracy of these flux uncertainty estimates: i) compare with the known uncertainties in the spectra from papers where this information is available: Hernán-Caballero et al. (2009), Yan et al. (2007), Menéndez-Delmestre et al. (2009) and Murphy et al. (2009); ii) compare with the RMS noise of the continuum in spectra that are plotted without smoothing (e.g. Weedman et al. 2005; Lutz et al. 2008; Pope et al. 2008; Zakamska et al. 2008).

Both approaches indicate that our flux uncertainty estimates are correct within a factor 2 in most sources. Even if a higher accuracy would be desirable, the statistical results drawn from the sample are little, if at all, affected. For an in-depth analysis of individual targets authors should use instead the latest version of the data products available at the *Spitzer* archive.

4 MEASUREMENTS

We provide measurements for several MIR spectral features that are commonly used to estimate the star-formation or nuclear activity, their relative contribution to the energy output of extragalactic sources or the amount of obscuration; namely PAH features, the 10 μm silicate feature and rest-frame monochromatic luminosities.

4.1 PAH features

PAH emission is a key tracer of star formation, with the luminosity of the PAH bands frequently used as an indirect estimator of the Star Formation Rate (SFR; e.g. Rigopoulou et al. 1999; Peeters et al. 2004; Brandl et al. 2006; Farrah et al. 2008) while their ratios relate to the ionization field in the interstellar medium (Draine & Li 2001; Rapacioli et al. 2005; Brandl et al. 2006; Galliano et al. 2008). For nearby galaxies with strong PAH bands and high signal-to-noise (S/N) spectra, it is possible to perform a detailed modelling of the continuum and Lorentzian profiles of the PAH bands (e.g. Smith et al. 2007; Treyer et al. 2010). For higher redshift sources, a similar analysis can be performed, provided adaptations are made to account for AGN emission and dust extinction (e.g. Sajina et al. 2007; Hernán-Caballero et al. 2009), but as the equivalent width (EW) of the feature, the S/N of the spectrum and the wavelength coverage decrease, degeneracy among solutions quickly becomes a major source of uncertainty. Simpler methods such as spline or linear interpolation of the local continuum and integration in the PAH band (e.g. Genzel et al. 1998; Rigopoulou et al. 1999; Brandl et al. 2006; Spoon et al. 2007) are much more resistant to weak or noisy features, but significantly underestimate PAH luminosities due to losses at the wings of the Lorentzian profiles and overlap between adjacent PAH bands (Smith et al. 2007; Treyer et al. 2010).

As already mentioned, the basic idea behind this work is to apply the same procedure when measuring the various features across all samples. We therefore opted to use an intermediate approach, in which the continuum is locally interpolated and the feature flux is integrated in a narrow band, but both measurements are later corrected for the expected width and shape of the feature's profile.

The measurement proceeds as follows: we select two narrow, continuum bands at both sides of each PAH feature, and estimate the average flux, f_ν, in these bands. We perform a linear interpolation to estimate the continuum underlying the feature, and subtract it from the spectrum. Finally we integrate the residual in a band centered at the expected wavelength of the peak of the PAH feature to obtain the integrated PAH flux. In order to maximize the S/N in the integrated PAH flux and to reduce the uncertainty in the underlying continuum, we use a rather narrow integration band (which loses a significant fraction of the PAH flux in the wings of the profile) and place the continuum bands in its close vicinity, without trying to avoid contamination by the wings of the PAH feature (see parameter values in Table 3).

The bias introduced by this procedure is compensated by a correction factor on the assumption that the PAH profile is Lorentzian with a known full width half maximum (FWHM). We estimate the error that this procedure introduces by meassuring line and continuum fluxes in a set of model continuum+Lorentzian spectra covering a wide range of EW, FWHM, and S/N values. We find that a 10% increase in the FWHM causes a 5-6% drop in the PAH flux, with no observable dependency on the EW or S/N of the spectrum.

Uncertainties in the PAH flux and the underlying continuum for each source are estimated by performing Monte Carlo simulations. Finally, we estimate EWs of the PAH features dividing the integrated PAH flux by the interpolated continuum at the center of the feature, and convert PAH fluxes to luminosities assuming a concordance ΛCDM cosmology ($\Lambda = 0.7$, $\Omega = 0.3$ and $H_0 = 70$ km s^{-1} Mpc^{-1}).

Since this approach is not valid for the overlapping 7.7 and 8.6 PAH bands, we perform measurements only for the 6.2 and 11.3 μm PAH features (which incidentally are the most used for diagnostics). The 6.2 μm feature is measured in 587 sources, that at 11.3 μm in 577, and both of them together in 481 sources.

4.2 Silicates

The 10 μm silicate feature, which can appear in emission or absorption, provides insight into the geometry of the dust distribution along the line of sight of the star-forming regions or the active nucleus as well as the amount of obscuration (e.g. Imanishi & Maloney 2003; Sturm et al. 2005; Imanishi et al. 2007). As with the PAH bands, the main difficulty in estimating the strength of the 10 μm silicate feature is the identification of the underlying continuum. In sources with weak or no PAH emission, we interpolate linearly in log(λ), log(f_λ) between anchor points at restframe 8.1 and 14.0 μm; but whenever there is significant PAH emission ($r_{\rm PDR} > 0.1$, see §5), we substitute the first anchor point by 5.55 μm in order to avoid the distortion introduced by the wings of the 7.7 and 8.6 μm PAH features.

We subtract from the spectrum the interpolated continuum, and integrate the residual (silicate feature) in the 9-11 μm range. The sign of this quantity allows to determine whether the feature is in emission (integral > 0) or in absorption (integral < 0). The theoretical wavelength of the silicate peak is 9.7 μm, but it is known that in many quasars and Seyfert galaxies the feature peak is shifted to longer wavelengths when it appears in emission (e.g. Siebenmorgen et al. 2005; Netzer et al. 2007). In addition, many star-forming sources show strong emission in the S(3) 9.665 μm transition of molecular hydrogen, which contaminates the peak of the silicate absorption profile.

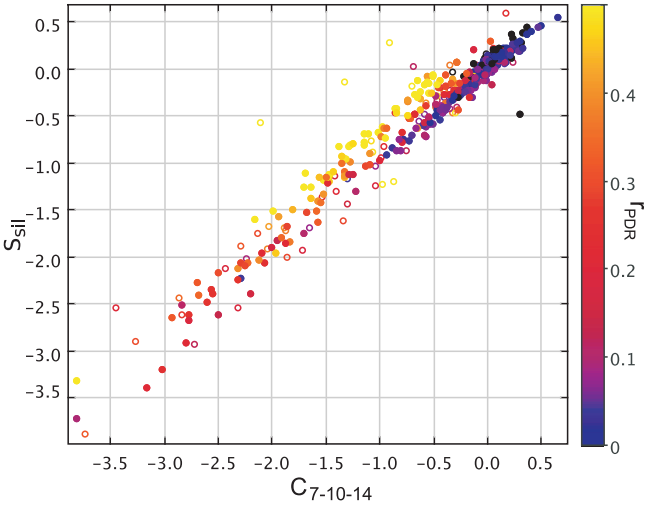

Figure 3. Comparison between two estimates of the silicate strength: $S_{\rm sil}$, obtained by the standard procedure (see text) and $C_{7-10-14}$, calculated as a three-band colour index. Sources with low uncertainties in the estimation of $S_{\rm sil}$ ($eS_{\rm sil} < 0.2$) are shown in filled circles, while open circles represent the remaining objects.

Since many spectra are too noisy to accurately measure where the peak of the silicate feature actually occurs, we simply assume it is located at $\lambda_p = 9.8$ μm for sources with silicate absorption and $\lambda_p = 10.5$ μm for silicate emission spectra. A detailed analysis of the 10 and 18 μm silicate features in the AGN-dominated sources of this sample, including measurement of the peak's wavelength, is the topic of a specialised study (Hernan-Caballero et al. in preparation).

The feature's peak flux density is used to calculate the silicate strength, $S_{\rm sil} = \ln[F(\lambda_p)/F_C(\lambda_p)]$. As in the PAH bands, uncertainties in the silicate parameters are estimated using Monte-Carlo simulations. $S_{\rm sil}$ measurements are obtained for 537 sources.

We also define the "three-band" colour index, $C_{7-10-14}$, as:

$$C_{7-10-14} = -2.5\, log\left(\frac{\sqrt{f_7 f_{14}}}{f_{10}}\right)$$

This parameter is an alternative, easily obtained estimator of the silicate strength, that shows a good correlation with $S_{\rm sil}$ in sources of all types (Figure 3).

In sources with little or no PAH emission, $S_{\rm sil}$ and $C_{7-10-14}$ are mostly interchangeable, while sources with strong PAH emission show a small but consistent bias towards $C_{7-10-14} < S_{\rm sil}$. This may be produced by a steeper slope of the starburst continuum component shortwards of ∼8.5 μm that decreases the interpolated 9.8 μm continuum for $S_{\rm sil}$ (and increases thus the $S_{\rm sil}$ value), and also from contamination by the wings of the 6.2 and 7.7 μm PAH features in the 7.0 μm flux, that reduces the $C_{7-10-14}$ estimate. The difference, $\Delta_{\rm sil} = S_{\rm sil} - C_{7-10-14}$ increases with the strength of the starburst component as measured by $EW_{6.2}$, and can be as high as ∼ 0.5 in extreme cases.

4.3 Monochromatic luminosities

Rest-frame monochromatic luminosities, $\nu L\nu$, allow for the comparison of spectral energy distributions of sources at different redshift without the need for K-corrections. We estimate them based on the IRS spectra at rest-frame wavelengths: 2.2, 3.6, 5.6, 7.0, 9.0, 10.0, 12.0, 14.0, 15.0, 18.0, 20.0 and 25.0 μm. To this end, each rest frame spectrum is integrated in a narrow band (between 0.5 and 2.0 μm wide depending on the wavelength) centered at the nominal wavelength, and divided by the band width. Table 2 summarizes these measurements.

Rest frame MIR colours and colour indices are also calculated and tabulated. Such quantities give a quick but accurate idea of the shape of a spectrum. The [5.6-15] μm colour, for instance, is a proxy for MIR continuum slope, while the three-band 7-10-14 μm colour index ($C_{7-10-14}$) can be used as a substitute estimate of the silicate strength in noisy or poorly sampled spectra (see §4.2).

5 SPECTRAL DECOMPOSITION

Decomposition of MIR spectra in several spectral components is a powerful tool that can provide considerable insight into the physics of the sources (e.g. Laurent et al. 2000; Tran et al. 2001).

MIR emission from active and star-forming galaxies arises mostly from HII regions, Photodissociation Regions (PDRs) and hot dust heated by energetic X-ray-to-UV photons from an AGN, so we have used a simple model comprising the superposition of three spectral templates (HII, PDR and AGN) obscured by a screen of dust.

The spectral decomposition is performed by fitting the 5–15 μm restframe range of the spectrum to a parametrized $F_\lambda(\lambda)$ of the form:

$$F_\lambda(\lambda) = e^{-b\tau(\lambda)}\Big(a_1 f_{\rm AGN}(\lambda) + a_2 f_{\rm HII}(\lambda) + a_3 f_{\rm PDR}(\lambda)\Big) \quad (1)$$

where the free parameters (b, a_1, a_2, a_3) are calculated using a Levenberg–Marquardt χ^2-minimization algorithm. A single optical depth value is applied to the three spectral components, but for most sources the solution is almost identical when two optical depth values (one for the AGN and other for the PDR and HII components) are used, with an increased χ^2 value due to the extra free parameter.

$\tau(\lambda)$ is obtained from the Galactic Centre extinction law (Chiar & Tielens 2006), while $f_{\rm AGN}$ is represented by the IRS spectrum of the PG QSO 3C273 (Wu et al. 2009), $f_{\rm PDR}$ by the ISOCAM spectrum of a PDR in the reflection nebula NGC 7023 (Cesarsky et al. 1996a) and $f_{\rm HII}$ by the ISOCAM spectrum of M17 in the vicinity of OB stars (Cesarsky et al. 1996b). Uncertainties in the fit parameters are estimated using Monte-Carlo simulations.

We quantify the contribution, r, of each spectral component to the MIR spectrum as the ratio of its integrated luminosity to the total luminosity in the 5–15 μm restframe range, $r_{\rm AGN}$, $r_{\rm HII}$ and $r_{\rm PDR}$ for the AGN, HII and PDR components. Figure 5 shows the distribution of the three spectral components in the sample.

Only 235 of the 695 sources with available redshifts have IRS spectra covering the 5–15 μm spectral range in its entirety. In many local galaxies, the IRS spectrum starts at 5.2–5.5 μm, while in higher redshift sources the long wavelength end of the spectrum is often shortwards of 15 μm. Nevertheless, 379 spectra cover more than 95% of the 5–15 μm range, and 595 show coverage ratios above 60%.

To validate the results on sources with incomplete spectral coverage, we have performed test runs of the decomposition algorithm on the subsample with full 5.5–15 μm coverage, but restricting the fitting range to 5–13.5 μm, 5–12 μm, and 5–10.5 μm. For each spectral component, i, we define the change in the estimated share of the 5–15 μm luminosity as: $\Delta r_i = r_i' - r_i$, where r_i' is the value of r_i obtained when fitting in the restricted range.

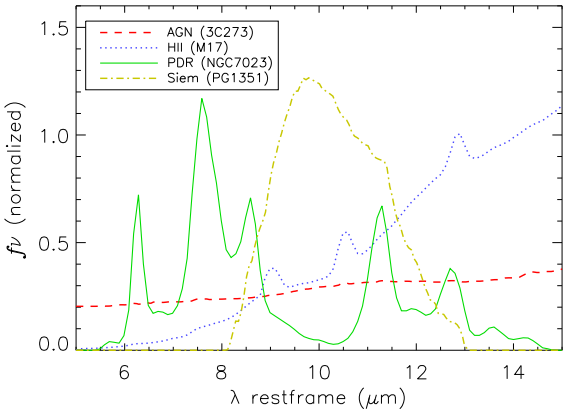

Figure 4. 5–15μm spectra of the AGN, HII and PDR templates used in the spectral decomposition. The silicate emission template used in the alternative spectral decomposition model for silicate emission sources is also shown.

The results (Table 4) show that decreasing the long wavelength limit to 13.5 μm has almost no effect, with typical Δr_i of a few percent, and no significant bias. A further reduction of the long wavelength limit down to 12 μm significantly reduces the contribution of the HII template, by 7 percentage points on average, and increases the dispersion in all components by a factor ~ 3. Nevertheless, moving the limit to 10.5 μm does not increase the bias, which improves sligthly for the HII and PDR templates; but the dispersion further increases by another factor ~ 2, to almost 0.2 for HII, which renders the decomposition results rather unreliable. Note that the HII component is by far the most affected by truncation of the spectrum at long wavelengths because of its steep slope.

$\Delta\tau_{9.7}$ also shows high dispersion for a 12 μm limit, but most of the strong deviations originate in spectra with poor S/N which show large parameter uncertainties even with full spectral coverage (Figure 6). There is no significant bias for $\Delta\tau_{9.7}$ except for the test in the 5–10.5 μm spectral range.

In order to obtain reliable measurements without sacrificing too many sources, we opt to require a lower limit of 60% coverage in the 5–10.5 μm spectral range to perform spectral decomposition. In addition, we provide coverage ratios for all sources in the sample.

Figure 7 shows $S_{\rm sil}$ versus the optical depth at 9.7 μm estimated from the b parameter ($\tau_{9.7}$) for the 379 sources with >95% coverage in the 5–15μm range.

The tight correlation and the significantly larger uncertainties in $S_{\rm sil}$ compared to $\tau_{9.7}$ are noteworthy. There appears to be a slope change at $S_{\rm sil}$ ~ -2, ($\tau_{9.7}$ ~ 3) that might be caused by saturation of the silicate feature: since $S_{\rm sil}$ depends on the 9.7 μm flux, it is difficult to obtain an accurate measurement when the flux level nears zero; also, emission in the 9.66 μm S(3) line of molecular hydrogen (found in many ULIRGs) can increase the measured 9.7 μm flux. On the contrary, $\tau_{9.7}$ takes advantage of the whole 5–15

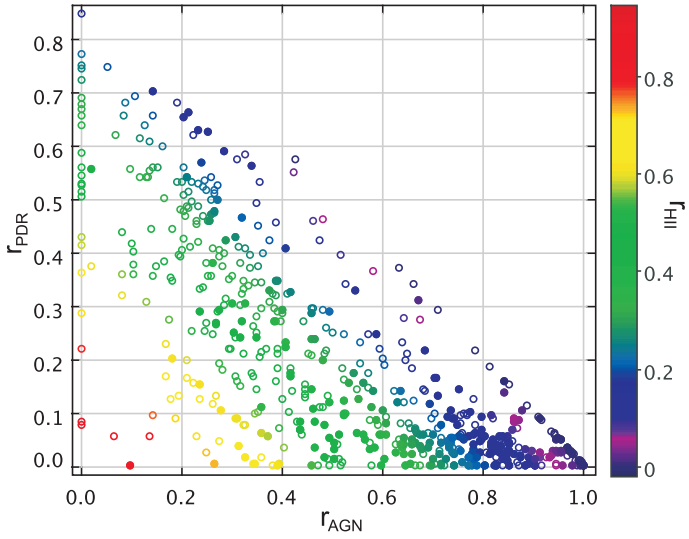

Figure 5. Contribution of PDR and AGN components to the integrated 5–15μm restframe luminosity as derived from the spectral decomposition. Filled symbols indicate sources with full 5.5-15 μm coverage in the IRS spectrum, while open symbols represent sources with only partial coverage. The amount of HII component can be calculated by the formula: r_{HII} = 1 - (r_{AGN}+r_{PDR}).

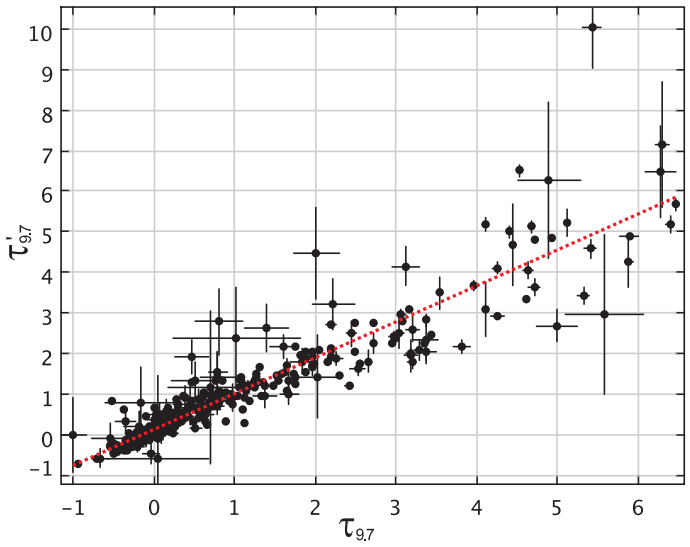

Figure 6. Comparison of decomposition $\tau_{9.7}$ values obtained by trimming spectral coverage to 5–12μm restframe (Y axis) versus $\tau_{9.7}$ obtained using the full 5–15 μm range (X axis). The dotted line represents a linear fit to the data.

μm spectrum, and we can obtain a sensible estimate of the 9.7 μm optical depth from the wings of the silicate profile, even if the feature is saturated.

When the silicate feature appears in emission, the best fit is obtained for a negative value of the opacity parameter *b*, since this produces a 10 μm bump with a shape alike that of the silicate emission feature. This unphysical solution allows for a decent fit of silicate emission sources with no extra parameters in the model, and the associated negative $\tau_{9.7}$ values correlate with S_{sil} values (Figure 7).

In order to check the validity of this approach, and to investigate the influence of a negative *b* value in the relative contribution of the three spectral components, we compare the results with an alternative spectral decomposition model for sources with the silicate feature in emission. In the alternative model, we fix the opacity parameter at $b = 0$ and include a fourth spectral template with the silicate emission profile of PG1351 (the source with the strongest silicate emission in the sample), obtained as the excess flux over the interpolated continuum between 8 and 13.5 μm. Figure 4 shows the 5–15 μm spectrum of the four components. The opacity needs to be fixed when using a silicate emission template to avoid degeneracies, since an increase in the silicate emission component can be compensated by a simultaneous increase in the opacity parameter.

To obtain a meassurement of the silicate strength we use the combined 9.7 μm flux of the AGN, HII and PDR templates as the continuum estimate (F_{cont}), and the 9.7 μm flux of the fourth (silicate) template as the peak flux estimate of the silicate feature (F_{sil}). The silicate strength is then calculated as $S^*_{sil} = \ln(1 + F_{sil}/F_{cont})$.

Comparison of S^*_{sil} with $\tau_{9.7}$ from the original decomposition model shows a good correlation, with significantly less dispersion than the correlation between S_{sil} and $\tau_{9.7}$ (Figure 7, inset plot). Comparison of S^*_{sil} with S_{sil} also yields a good correlation, with $S^*_{sil} \sim 0.91\ S_{sil}$. Changes in the relative contribution of spectral components, when adding the Silicate template, are small; in particular r_{PDR}, a parameter we will use for diagnostics in §6.2, is almost unaltered with a Δr_{PDR} averaging 0.0016 and a standard deviation of 0.012.

The alternative spectral decomposition model assumes the silicate feature peaks at ~9.8 μm, while there are instances in our sample where the peak of the emission is shifted towards longer wavelengths. These S_{sil} estimates should, therefore, be considered as an approximation to the real values. A more accurate meassurement would require the ability to shape and/or shift the silicate template in order to reproduce the diversity observed within the ATLAS sample. This and other issues related to the silicate feature in AGN will be addressed in a forthcoming work.

The luminosity of the PDR component estimated in the fit (L_{PDR}) is a measurement of the total PAH luminosity in the galaxy. Comparison of L_{PDR} with the 6.2 μm PAH luminosity (Figure 8) indicates the latter is responsible for roughly 10% of the total PAH luminosity in the galaxy, in agreement with the results of Smith et al. (2007) in a sample of local starbursts, and that this ratio does not significantly change in the higher luminosity sources.

A comparison of $EW_{6.2}$ with r_{PDR} shows significant dispersion (Figure 9), mostly because of variations in the relative strength of PAH features. Unusually low 6.2 μm to total PAH luminosity ratios ($L_{6.2}/L_{PDR} < 0.05$) are found mainly in heavyly obscured ULIRGs, where an absorption band of water ice overlaps with the 6.2μm PAH emission, while very high ratios ($L_{6.2}/L_{PDR} > 0.2$) appear in sources with peculiar MIR spectra that suggest unusual physical properties or artifacts in the data.

6 MIR DIAGNOSTICS

6.1 The fork diagram

The "fork diagram", i.e. the strength of the 10 μm silicate feature, S_{sil} , versus the equivalent width of the 6.2 μm PAH feature, $EW_{6.2}$, first discussed by Spoon et al. (2007), is now considered a standard tool to distinguish between AGN- and starburst-dominated

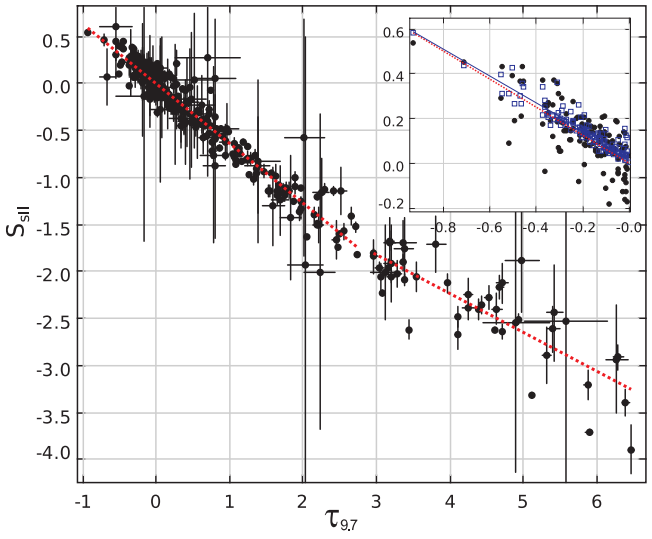

Figure 7. S_{sil} versus $\tau_{9.7}$ for the sources in the sample with complete 5.5–15 μm spectral coverage. Linear fits for sources with $\tau_{9.7} < 3$ and $\tau_{9.7} > 3$ are shown in dotted lines. The inset plot is a close up to the silicate emission region of the diagram where only sources with uncertainties in S_{sil} below 0.2 are shown, for clarity. The open blue squares are the S^*_{sil} estimates obtained from the alternative spectral decomposition model (see text), plotted as a function of $\tau_{9.7}$.

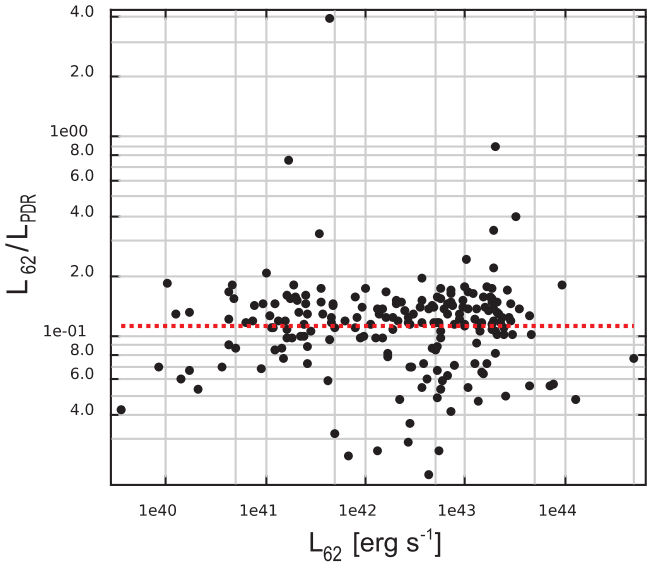

Figure 8. Ratio between the 6.2 μm PAH luminosity, as obtained by integration in the 5.95–6.55 μm band with corrections for flux lost in the wings of the profile (L_{62}), and the integrated PAH luminosity as derived from the PDR component in spectral decomposition (L_{PDR}) as a function of L_{62} for sources with a S/N > 2 detection of the 6.2 μm PAH feature. The dotted line represents the best fit linear relation.

sources (e.g. Farrah et al. 2007; Zakamska et al. 2008; Wu et al. 2009; Willett et al. 2010). Starbursts tend to have large values of $EW_{6.2}$, which decrease with increasing S_{sil} due to depletion of the PAH band by absorption of adjacent water ice bands (Spoon et al. 2002) and increased continuum emission, while in AGN-dominated galaxies silicates appear in shallower absorption (typically type 2 objects) or emission (type 1 objects) while the PAH features are less pronounced.

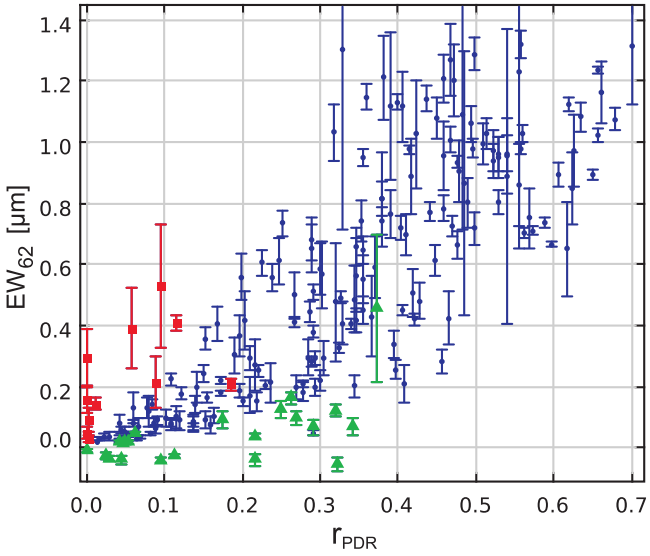

Figure 9. $EW_{6.2}$ versus r_{PDR} for the sources in the sample with a S/N > 2 detection of the 6.2 μm PAH feature. Symbols indicate the relative contribution of the 6.2 μm to the integrated PAH luminosity as meassured by the L_{62}/L_{PDR} ratio: red squares indicate a ratio larger than 0.2, while green triangles mark ratios smaller than 0.05.

A variant of the fork diagram can be obtained using the 11.3 μm PAH feature instead of the 6.2 μm one (Figure 10). This approach has the advantage of requiring less wavelength coverage and avoids the bias introduced in deeply obscured sources by water ice absorption in the wings of the 6.2 μm PAH feature (note that the 11.3 μm flux can be heavyly depleted by silicate absorption, but since the silicate feature is very broad, the equivalent width is not significantly altered). In this variant of the diagram the starburst-dominated branch turns nearly vertical, but the topology remains unchanged.

The parameters derived from the spectral decomposition allow us to build an alternative fork-like diagram, where r_{PDR} substitutes the PAH EW and $\tau_{9.7}$ takes the place of S_{sil} (Figure 11). The advantage of this procedure is the results do not depend on the measurement of a single PAH band and the flux at the core of the silicate feature and the related caveats; instead, it uses the whole 5–15 μm spectrum, making it less vulnerable to noise.

6.2 MIR classification

We use the spectral decomposition results to obtain a MIR classification of the sources in the ATLAS sample. At a first stage, we separate AGN-dominated and starburst-dominated sources based on the fraction of PDR component, r_{PDR}.

We set the limit between AGN-dominated and starburst-dominated sources at $r_{PDR} = 0.15$, which corresponds to $EW_{6.2} \sim 0.2$ μm according to the relation shown in Figure 9.

Hernan-Caballero et al. (2009) showed that typical $\nu L_\nu(5.5\mu m)/L_{IR}$ratios for AGN have values around 0.3 (their Figure 13), and starburst sources have mean L_{62}/L_{IR}ratios of 0.01 (their Table 9). Aproximating the 6.2 μm continuum with the 5.5 μm luminosity would imply an equivalent width of $EW_{6.2} \sim 0.2$

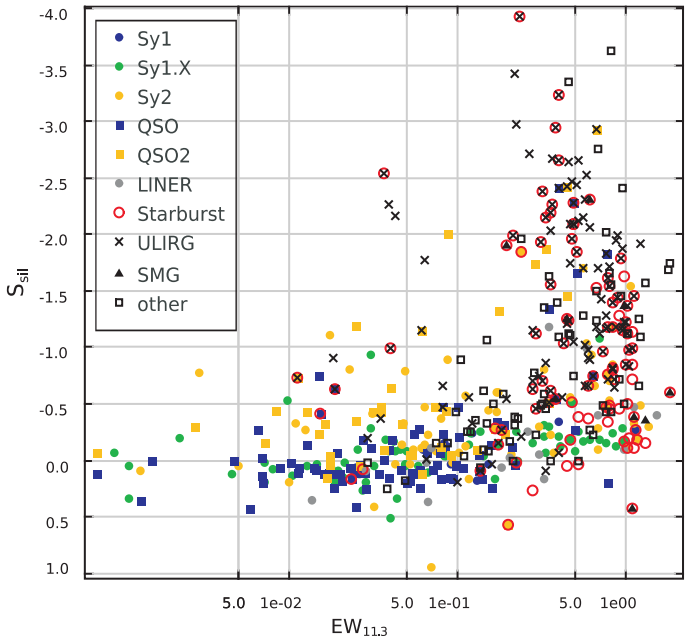

Figure 10. Fork Diagram showing the 10 μm silicate strength versus the 11.3 μm PAH equivalent width. Symbols indicate the classification of sources in the literature. Solid symbols indicate optical AGN classification as Seyfert 1 (blue circles), Seyfert 2 (yellow circles), intermediate Seyfert types (green circles), LINER (grey circles), quasar (blue boxes) and type 2 quasar (yellow boxes); red open circles indicate Starburst or HII-region type in the optical, while black crosses and triangles represent ULIRGs and submillimiter galaxies, respectively. Sources not classified, or with types that do not match any of the former ones are shown in black open squares.

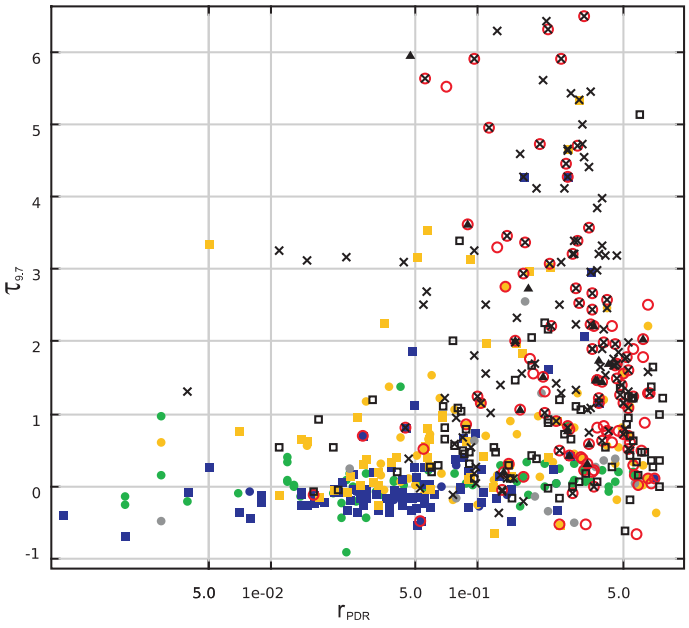

Figure 11. Analog to the fork diagram obtained by representing the fraction of PDR component r_{PDR} versus the optical depth at 9.7 μm, $\tau_{9.7}$, as calculated with the spectral decomposition method. Symbols as in Fig. 10.

μm for a source with 50% starburst and 50% AGN contribution to the IR luminosity.

Since many spectra are noisy and there is a significant number of sources near this threshold, we require the 1-σ confindence interval not to contain the threshold value in order to qualify as AGN-dominated or starburst-dominated. The remaining sources are classified as "composites" if r_{PDR} has S/N > 2 or "unknown" otherwise.

In 93 sources the spectral coverage in the 5–15μm range is too low to estimate r_{PDR}, but the equivalent width of the 6.2 or 11.3 μm PAH features is meassured. For these sources we use $EW_{11.3}$ = 0.2 μm (or $EW_{6.2}$ = 0.2 μm) as an alternative boundary between the starburst-dominated and AGN-dominated classes.

With these criteria, 257 sources are classified as starburst-dominated in the MIR (MIR_SB), 348 as AGN-dominated (MIR_AGN) and 29 are too close to the threshold to decide, so they get classified as composites (MIR_COMP). The spectra of another 49 sources are too noisy to tell, and in the remaining 12 the 6.2 and 11.3 PAH features are both outside of the observed spectral range.

The 348 AGN-dominated sources are further sub-classified according to their $\tau_{9.7}$ meassurement into silicate emission (MIR_AGN1, 119 sources) or absorption (MIR_AGN2, 160 sources), again requiring the 1-σ confidence interval in $\tau_{9.7}$ not to cross $\tau_{9.7}$ = 0 for a clean classification. Sources in which the 1-σ interval contains $\tau_{9.7}$ = 0, but with uncertainties below 0.1 are classified as "flat MIR-spectrum AGN" (MIR_AGNx, 18 sources) to indicate that there is no strong emission or absorption at 10 μm, and the remaining 51 sources retain the generic MIR_AGN classification.

Table 5 shows the distribution of sources in the sample according to their optical spectroscopic and MIR classifications. Values indicate the number of sources with a given optical and MIR classification. Sources classified in the literature as both AGN and starburst in the optical are discarded for clarity, but the counts that would be obtained were they included, are shown in brackets.

In most sources, the optical and MIR classifications are broadly consistent with each other (i.e., type 1 AGN usually show strong continuum and silicate emission, type 2 show also strong continuum and silicate absorption, and starbursts show strong PAH features on top of a fainter continuum), but there are exceptions. In particular, more than 1/4 of Seyfert 1s and QSOs show significant silicate absorption, and many sources classified as AGN in the optical are starburst dominated in the MIR. Apperture effects may be at least in part responsible for this, since the IRS spectrum of a galaxy nucleus include a far larger share of the emission from the galaxy compared to the corresponding optical spectrum.

In the lower luminosity Seyferts, the host galaxy can contribute by a large fraction to the luminosity within the IRS slit, and composition of the (AGN-dominated) nuclear spectrum and (starburst-dominated) host galaxy spectrum can produce a silicate feature in absorption. This interpretation is supported by the strong PAH features observed in some Seyferts, that make them qualify as starburst-dominated in the MIR. Nevertheless, significant silicate absorption is also present in the spectrum of several QSOs, where the contribution from the host galaxy to the MIR luminosity is expected to be small. Thus at least in some cases the silicate absorption feature may be caused by obscuration of the AGN emission, be it in a dusty torus or in the host galaxy.

On the other hand, there are also 15 Seyfert 2s and QSO2s (1/6 of the total) with the silicate in emission, as meassured by $\tau_{9.7}$ (12 of them also confirmed by $S_{sil} > 0$).

These apparent discrepancies, however, can not be regarded as evidence against the unified model of AGN; in fact, such behaviour

is predicted by both smooth and clumpy circumnuclear dust distribution models. Smooth models predict silicate absorption in compact, high opacity face-on tori (Fritz et al. 2006), and also allow for silicate emission in type 2 AGN (e.g. Hatziminaoglou et al. 2008). Clumpy models require a high number of clouds along the equator and high optical depth to produce silicate absorption in type 1 AGN (Nenkova et al. 2008), while some parameter combinations could give rise to silicate emission in type 2 AGN (e.g. Nikutta et al. 2009).

We therefore conclude that a silicate emission or absorption feature is not a reliable indicator, on its own, of the optical spectral type.

There are also four LINERs with silicate emission, three of them show broad Balmer lines, and a strong silicate peak, while the remaining one is a radiogalaxy with a weaker silicate feature.

Almost all optical starbursts are also classified as starbursts in the MIR, but the opposite is not true: roughly half of MIR starbursts belong to some of the optical AGN classes. These sources are mostly nearby galaxies harbouring low luminosity AGN, that can be outshined by the galaxy in the large IRS aperture. When taking into account only objects at $z > 0.1$, from 98 MIR_SB sources 54 are classified as starbursts in the optical, while 31 have LINER cores and only 13 are Seyferts or QSOs.

7 AVERAGE TEMPLATES

A number of synthetic galaxy templates have been obtained from the average spectrum of populations matching certain criteria, shown in Table 6.

We obtain average templates for Seyfert 1, Seyfert 1.X, Seyfert 2, LINER, QSO, QSO2, starburst, ULIRGs and SMGs. ULIRGs with LINER or starburst cores are discarded when composing the LINER and starburst templates, that include only sources with $\nu L_\nu(7\mu m) < 10^{44}$ erg s^{-1}. Three additional templates are generated for sources classified in the MIR as dominated by starburst (MIR_SB), unobscured AGN (MIR_AGN1) and obscured AGN (MIR_AGN2).

The individual spectra are normalized at 7 μm resframe and resampled to a common grid of wavelength values. The highest and lowest flux values in each wavelength bin are discarded, and the remaining ones are averaged with the arithmetic mean to obtain the template flux. The 12 templates obtained are shown in Figure 12. Shaded areas indicate the 1-σ dispersion of individual spectra, which is higher at longer wavelengths because of slope variations among sources of the same type. These templates are available as ASCII tables with columns for rest frame wavelength, normalized average flux density, 1-σ dispersion in flux density and number of sources contributing to the average for each wavelength bin.

The QSO template (*e*) is flat and almost featureless, while the type 2 QSOs (*f*) have on average a redder continuum and a somewhat pronounced silicate feature in absorption. The equivalent with of the PAH features in the QSO and QSO2 templates are much lower compared to those present in the average Sy1 (*a*) and Sy2 (*c*) templates, in spite of the high star formation rates derived from both the PAH features (e.g. Hernán-Caballero et al. 2009) and FIR luminosities (e.g. Hatziminaoglou et al. 2010), because the strong continuum emission from the AGN masks the underlying emission from the host galaxy. The LINER template (*d*) includes only nearby sources and its low PAHs equivalent widths are indicative of weak circumnuclear star formation. Its 5–9 μm continuum is bluer than either the starburst or Seyfert templates because contribution from starlight is not negligible compared to the AGN emission. Complementary templates are generated for all sources classified as ULIRG (*h*) in the literature (irrespective of their optical spectral type) as well as the SMGs (*i*). The latter has a very limitted spectral coverage, as all the objects composing the SMG sample are high-redshift objects (with an average redshift $\langle z \rangle = 1.93$).

The MIR AGN average templates (*j*, *k*) also show interesting characteristics: the objects selected to have silicate in emission at 10 μm have a flat spectrum with the silicate feature at 18 μm clearly in emission, as well. The objects selected to have the silicate feature in absorption have a redder continuum and show no feature at 18 μm, be it in emission or in absorption. In a detailed comparative study between smooth and clumpy dust distributions, Fetre et al (in prep) show that such silicate features' behaviour is compatible with both clumpy and smooth dust distributions and hence we can not derive any constraints from the average templates.

Interestingly, the average starburst template constructed from objects selected as such in the optical (*g*) shows more prominent PAH features and a redder continuum than the equivalent MIR template (*l*). This difference is most likely due to the different nature of the objects composing the two samples. The optical sample consists of low redshift starburst galaxies alone, while the MIR template has a higher average redshift, includes many ULIRGs as well as objects with significant AGN contribution.

8 CONCLUSIONS

We have collected a sample of 739 active and starburst galaxies with *Spitzer*/IRS spectra from the literature. The sample, though not statistical, comprises a variety of objects, namely type 1, 2 QSOs and Seyfert galaxies, intermediate Seyfert galaxies, ULIRGs, starburst and sub-mm galaxies, with a large span of spectral properties such as PAH and silicate features, continua and distinct physical characteristics, and is the largest of its kind compiled to date. MIR properties were computed in a concise way for all objects and can thus be directly compared among the various types of objects.

We find that the silicate strength, $S_{\rm sil}$, a meassurement of the intensity of the 10 μm silicate feature that takes positive (negative) values when the feature is in emission (absorption), is well aproximated by a "three band" color index, $C_{7-10-14}$, that is usually easier to obtain, except for sources with strong PAH emission that contaminates the flux at 7 μm, causing $C_{7-10-14}$ to consistently lie short of $S_{\rm sil}$. A more elaborate meassurement of dust obscuration, $\tau_{9.7}$, obtained from the scaling factor applied to the extinction law in a spectral decomposition analysis, shows also a tight correlation with $S_{\rm sil}$, but with different slopes for sources with saturated ($\tau_{9.7} > 3$) and unsaturated ($\tau_{9.7} < 3$) silicate features.

We find that the ratio of the PDR component to the total luminosity of each object, integrated between 5 and 15 μm restframe, $r_{\rm PDR}$, and $\tau_{9.7}$, both obtained from the spectral decomposition, provide better AGN versus SB and obscuration diagnostics than the usual PAH EW and $S_{\rm sil}$ in sources with sufficient spectral coverage, as they do not depend on a single spectral feature and thus are less vulnerable to noise. Most QSOs and Seyfert1 galaxies show $\tau_{9.7}$ values clustered around zero and $r_{\rm PDR}$ values below 0.15, while starburst galaxies have large $r_{\rm PDR}$ values and moderate to deep silicate absorption (higher in the starburst ULIRGs than in lower luminosity starbursts). Type 2 QSOs and Seyfert 2s exhibit low $r_{\rm PDR}$ values and usually silicate absorption, sometimes strong, while LINERs can have almost any combination of parameters, due to their nature and definition.

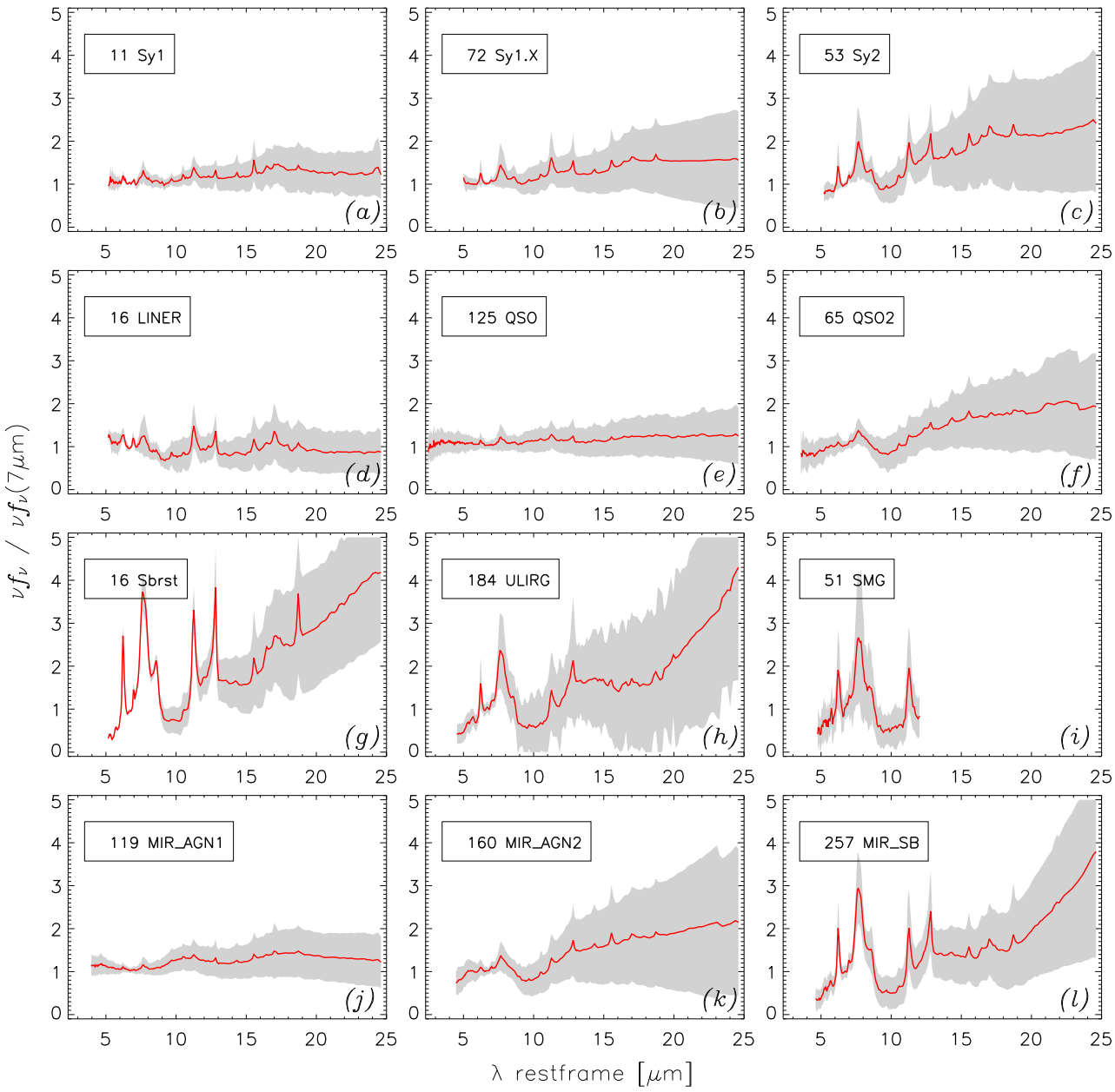

Figure 12. Composite templates for subsamples of the ATLAS sample. In the first three rown, sources are selected based on their optical type and MIR luminosity, except for the ULIRG and SMG templates (see text). The bottom row shows average templates of the sources grouped according to the MIR classification.

We then derive a simple classification of the sources, based on the values of $r_{\rm PDR}$ and $\tau_{9.7}$. Objects with $r_{\rm PDR} < 0.15$ are considered to be AGN-dominated, while $r_{\rm PDR} > 0.15$ indicates starburst-dominated sources, and the AGN-dominated subsample is further divided into silicate emitters and absorbers ($\tau_{9.7} > 0$ and $\tau_{9.7} < 0$, respectively). Comparison of this simple MIR classifications with the optical classifications in the literature is not straight forward, since the much wider apperture of the IRS slit with respect to optical spectroscopy allows for a larger fraction of the host galaxy in the MIR spectrum of resolved sources. Nevertheless, optical and MIR classifications are broadly consistent. Apperture effects may explain the larger fraction of starburst-dominated sources in the MIR relative to optical classifications, and the composition of nuclear and host galaxy spectra might account for some of the type 1 Seyfert galaxies that exhibit silicate absorption, even if in higher luminosity QSOs a source of obscuration (whether in a circumnuclear dusty torus or in the host galaxy) is required to explain the cases of silicate absorption. Since up to 1/4 of the type 1 AGN show silicate absorption and 1/6 of type 2 AGN show silicate emission, we conclude the silicate feature is not, on its own, a reliable indicator of the AGN optical type.

All spectra in the sample, the average templates, as well as ancillary data, including (but not limited to) optical, IR and radio photometry, redshifts, and MIR spectral meassure-

ments are made available to the public at the ATLAS website: http://www.denebola.org/atlas.

ACKNOWLEDGEMENTS

This work is based on observations made with the *Spitzer Space Telescope*, which is operated by the Jet Propulsion Laboratory, Caltech under NASA contract 1407.
This work made use of the software TOPCAT (http://www.star.bris.ac.uk/~mbt/topcat/) developed by M. Taylor.
We wish to thank Jorge A. Pérez Prieto for his kind assistance with the ATLAS web site, and the anonymous referee for the very useful comments and suggestions.

REFERENCES

Brand K. et al., 2008, ApJ, 680, 119
Brandl, B. R. et al., 2006, ApJ, 653, 1129
Buchanan C., Gallimore J., O'Dea C., Baum S., Axon D., Robinson A., Elitzur M., Elvis M., 2006, AJ, 132, 401
Cao C., Xia X. Y., Wu H., Mao S., Hao C. N., Deng Z. G., 2008, MNRAS, 390, 336
Clavel J., Schulz B., Altieri B., Barr P., Claes P., Heras A., Leech K., Metcalfe L., Salama A., 2000, A&A, 357, 839
Cesarsky D., Lequeux J., Abergel A.,Perault M., Palazzi E., Madden S., Tran D., 1996a, A&A, 315, 305
Cesarsky D. et al., 1996b, A&A, 315, L309
Chiar J. E., Tielens A. G. G. M., 2006, ApJ, 637, 774
Dasyra K. M. et al., 2009, ApJ, 701, 1123
Deo R. P., Crenshaw D. M., Kraemer S. B., Dietrich M., Elitzur M., Teplitz H., Turner T. J., 2007, ApJ, 617, 124
Draine B. T., Li A., 2001, ApJ, 551, 807
Farrah D. et al., 2007, ApJ, 667, 149
Farrah D. et al., 2008, ApJ, 677, 957
Farrah D., Weedman D., Lonsdale C. J., Polletta M., Rowan-Robinson M., Houck J., Smith H. E. 2009, ApJ, 696, 2044
Fritz J., Franceschini A., Hatziminaoglou E. 2006, MNRAS, 366, 767
Galliano F., Madden S. C., Tielens A. G. G. M., Peeters E., Jones A. P., 2008, ApJ, 679, 310
Genzel R. et al., 1998, ApJ, 498, 579
Haas M., Siebenmorgen R., Schulz B., Krügel E., Chini R. 2005, A&A, 442, L39
Hao L. et al., 2005, ApJ, 625, L75
Hao L., Weedman D. W., Spoon H. W. W., Marshall J. A., Levenson N. A., Elitzur M., Houck J. R., 2007, ApJ, 655, L77
Hatziminaoglou E. et al., 2005, AJ, 129, 1198
Hatziminaoglou E. et al., 2008, MNRAS, 386, 1252
Hatziminaoglou E., Fritz J., Jarrett T., 2009, MNRAS, 399, 1206
Hatziminaoglou E. et al., 2010, A&A, 518, L33
Hernán-Caballero A. et al. 2009, MNRAS, 395, 1695
Hiner K. D., Canalizo G., Lacy M., Sajina A., Armus L., Ridgway S., Storrie-Lombardi Lisa. ApJ, 706, 508
Imanishi M., Maloney P. R., 2003, ApJ, 588, 165
Imanishi M., Dudley C. C., Maiolino R., Maloney P. R., Nakagawa T., Risaliti G., 2007, ApJS, 171, 72
Imanishi M. 2009, ApJ, 694, 751
Imanishi M., Maiolino R., Nakagawa T. 2010, ApJ, 709, 801
Lacy M. et al., 2004, ApJS, 154, 166
Lacy M. et al., 2007, ApJ, 669, 61
Laurent O., Mirabel I. F., Charmandaris V., Gallais P., Madden S. C., Sauvage M., Vigroux L., Cesarsky C., 2000, A&A, 359, 887
Leipski C. et al., 2009, ApJ, 701, 891
Lutz D. Spoon H. W. W., Rigopoulou D., Moorwood A. F. M., Genzel R., 1998, ApJ, 505, 103L
Lutz D. et al., 2008, ApJ, 684, 853L
Maiolino R., Shemmer O., Imanishi M., Netzer H., Oliva E., Lutz D., Sturm E., 2007, A&A, 468, 979
Marconi A., Risaliti G., Gilli R., Hunt L. K., Maiolino R., Salvati, M., 2004, MNRAS, 351, 169
Menéndez-Delmestre K. et al., 2009, ApJ, 699, 667
Murphy E. J., Chary R. R., Alexander D. M., Dickinson M., Magnelli B., Morrison G., Pope A., Teplitz H. I., 2009, ApJ, 698, 1380
Nenkova M., Ivezic Z., Elitzur M., 2002, ApJ, 570, 9
Nenkova M., Sirocky M.M., Ivezic Z., Elitzur M., 208, ApJ, 685, 147
Netzer H. et al., 2007, ApJ, 666, 806
Nikutta R., Elitzur M., Lacy M., 2009, ApJ, 707, 1550
Peeters E., Spoon H. W. W., Tielens A. G. G. M., 2004, ApJ, 613, 986
Polletta M., Weedman D., Hönig S., Lonsdale C. J., Smith H. E., Houck J., 2008, ApJ, 675, 960
Pope A. et al., 2008, ApJ, 675, 1171
Rapacioli M., Joblin C., Boissel P., 2005, A&A, 429, 193
Rigopoulou D., Spoon H. W. W., Genzel R., Lutz D., Moorwood A. F. M., Tran Q. D., 1999, AJ, 118, 2625
Sajina A., Yan L., Armus L., Choi P., Fadda D., Helou G., Spoon H. W. W., 2007, ApJ, 664, 713
Schweitzer M. et al., 2006, ApJ, 649, 79
Shi Y. et al., 2006, ApJ, 653, 127
Shi Y. et al., 2007, ApJ, 669, 841
Siebenmorgen R., Haas M., Krügel E., Schulz B., 2005, A&A, 436, 5L
Siebenmorgen R., Krügel E., Spoon H.W.W., 2004, A&A, 414, 123
Smith J. D. T. et al., 2007, ApJ, 656, 770
Spoon H., Keane J., Tielens A., Lutz D., Moorwood A., Laurent O., 2002, A&A, 385, 1022
Spoon H. W. W., Marshall J. A., Houck J. R., Elitzur M., Hao L., Armus L., Brandl B. R., Charmandaris V., 2007, ApJ, 654, 49
Stern D. et al., 2005, ApJ, 631, 163
Sturm E. et al., 2000, A&A, 358, 481
Sturm E. et al., 2005, ApJ, 629, 21
Sturm E., Hasinger G., Lehmann I., Mainieri V., Genzel R., Lehnert M. D., Lutz D., Tacconi L. J., 2006, ApJ, 642, 81
Teplitz H. I. et al., 2006, ApJ, 638, L1
Tommasin S., Spinoglio L., Malkan M. A., Smith H., González-Alfonso E., Charmandaris V. 2008, ApJ, 676, 836
Tran Q. D. et al., 2000, ApJ, 552, 527
Treyer M. et al. 2010, ApJ, 719, 1191
Valiante E., Lutz D., Sturm E., Genzel R., Tacconi L. J., Lehnert M. D., Baker A. J. 2007, ApJ, 660, 1060
Véron-Cetty M.P., Véron P., 2006, A&A, 455, 773
Weedman D. W. et al., 2005, ApJ, 633, 706
Weedman D. W. et al., 2006a, ApJ, 651, 101
Weedman D. W. et al., 2006b, ApJ, 653, 101
Weedman D. W. et al., 2009, ApJ, 693, 370
Willett K. W., Stocke J. T., Darling J., Perlman E. S. 2010, ApJ, 713, 1393

Wu Y., Charmandaris V., Huang, J., Spinoglio, L., Tommasin, S. 2009, ApJ, 701, 658
Yan L. et al., 2007, ApJ, 658, 778
Zakamska N. L., Gómez L., Strauss M. A., Krolik J. H. 2008, AJ, 136, 160

This paper has been typeset from a TEX/ LATEX file prepared by the author.

Table 1. IRS observations log

Sample	IRS modules	Spitzer Archive PID(s)	Comments
Brand et al. 2008, ApJ, 680, 119	SL1,LL2,LL1	15	16 optically faint QSOs with X-ray detection
Brandl et al. 2006 , ApJ, 653, 1129	SL,LL	14	22 nearby starbursts
Buchanan et al. 2006, AJ, 132, 401	SL2-LL1 (map)	3269	87 nearby 12um-selected Seyfert galaxies
Cao et al. 2008, MNRAS, 390, 336	SL,LL	various	19 ultraluminous IR QSOs
Dasyra et al. 2009, ApJ, 701, 1123	SL1,LL2,LL1*	20629	150 24μm selected IR-luminous galaxies
Deo et al. 2007, ApJ, 671, 124	SL,LL	3374	12 Seyfert 1.8 and 1.9 galaxies
Farrah et al. 2009, ApJ, 696, 2044	SL1,LL2,LL1*	30364	16 optically faint 70 μm sources
Haas et al. 2005, A&A, 442, L39	SL,LL	3349	7 quasars and 7 radio galaxies
Hao et al. 2005, ApJ, 625, L75	SL,LL	14	5 PG quasars
Hernán-Caballero et al. 2009, MNRAS, 395, 1695	SL,LL	3640	69 15um-selected IR-luminous galaxies
Hiner et al. 2009 , ApJ, 706, 508	SL,LL	20083	6 type 1 and 7 type 2 MIR selected quasars
Imanishi et al. 2007, ApJ, 171, 72	SL,LL	105,2306,3187	buried AGN in IR galaxies
Imanishi et al. 2009, ApJ, 694, 751	SL,LL	105,30407,20589	20 buried AGN in IR galaxies
Imanishi et al. 2010, ApJ, 709, 801	SL,LL	50008,3187,30407	17 nearby ULIRGs
Lacy et al. 2007, ApJ, 669, 61	SL1,LL2	20083	6 type 2 quasars
Leipski et al. 2009, ApJ, 701, 891	SL,LL	20525	25 FR-I radio galaxies
Lutz et al. 2008, ApJ, 684, 853	LL	30314	12 z∼2 mm-bright type 1 quasars
Maiolino et al. 2007, A&A, 468, 979	LL1	20493	4 high luminosity quasars 2<z<3.5
Menéndez-Delmestre et al. 2009, ApJ, 699, 667	LL1,LL2*	20081	24 submm galaxies
Murphy et al. 2009, ApJ, 698, 1380	SL1,LL2,LL1	20456	22 galaxies in GOODS-N
Netzer et al. 2007 ApJ, 666, 806	SL,SH,LH	3187	23 Palomar Green QSOs
Polletta et al. 2008, ApJ, 675, 960	SL1,LL2,LL1	various	21 obscured AGNs
Pope et al. 2008, ApJ, 675, 1171	LL2,LL1*	20456,20081	13 submm galaxies
Shi et al. 2006, ApJ, 653, 127	SL,LL	various	68 AGN
Siebenmorgen et al. 2005, A&A, 436, L5	SL,LL	20231	3C 249.1, 3C 351
Sturm et al. 2005, ApJ, 629, L21	SL,SH,LH	3237	NGC 3998
Sturm et al. 2006, ApJ, 642, 81	SL,LL*	3223	7 X-ray selected type 2 quasars
Tommasin et al. 2008, ApJ, 676, 836	SH,LH	30291	29 Seyfert galaxies
Valiante et al. 2007, ApJ, 660, 1060	SL,LL*	3241	9 submm galaxies
Weedman et al. 2005, ApJ, 633, 706	SL,LL,SH,LH	14	8 AGN
Weedman et al. 2006a, ApJ, 651, 101	SL1,LL2,LL1*	12,15	24 optically faint 24 μm selected AGN
Weedman et al. 2006b, ApJ, 653, 101	SL1,LL2,LL1*	15	11 AGN and 9 starbursts
Weedman et al. 2009, ApJ, 693, 370	SL,LL*	40038,20128,20083,40539	24 AGNs and some starbursts
Willett et al. 2010, ApJ, 713, 1393	SL,LL,SH,LH	30515,50591,105	8 compact radio galaxies
Wu et al. 2009, ApJ, 701, 658	SL,LL (map)	various	103 Seyfert galaxies
Yan et al. 2007, ApJ, 658, 778	SL1,LL2,LL1*	3748	52 24 μm seleted sources
Zakamska et al. 2008, AJ, 136, 160	SL1,LL2	105,3163	12 QSO2s from SDSS

*not all targets observed in all modules

Table 2. monochromatic luminosity meassurement parameters

band name	λ_{rest} [μm]	bandwidth [μm]	$N_{sources}$
K	2.2	0.2	29
3.6	3.6	0.2	102
5.6	5.55	0.5	485
7	7.0	0.5	630
9	9.0	0.5	656
10	10.0	1.0	624
12	12.0	1.0	565
14	14.0	1.5	508
15	15.0	1.5	489
18	18.0	1.5	430
20	20.0	1.5	397
25	25.0	2.0	352

Table 3. PAH meassurement parameters

	6.2μm PAH	11.3μm PAH
central wavelength	6.25	11.3
integration band	6.0-6.5	11.05-11.55
continuum intervals	5.8-6.0,6.5-6.7	10.75-11.0,11.65-11.9
assumed FWHM	0.2	0.2

Table 4. Bias in decomposition parameters caused by incomplete spectral coverage

	5.0–13.5μm		5.0–12.0μm		5.0–10.5μm	
	mean	σ	mean	σ	mean	σ
$\Delta r_{\rm AGN}$	0.0029	0.017	0.0426	0.051	0.0590	0.118
$\Delta r_{\rm HII}$	-0.0081	0.034	-0.0699	0.098	-0.0499	0.193
$\Delta r_{\rm PDR}$	0.0052	0.029	0.0272	0.065	-0.0092	0.096
$\Delta\tau_{9.7}$	-0.0005	0.141	0.0027	0.560	0.2723	0.820

Table 5. Comparison of optical and MIR classifications

	MIR_AGN1	MIR_AGNx	MIR_AGN2	MIR_AGN	MIR_COMP	MIR_SB
Sy1	7	0	3	0	0	1(2)
Sy1.X	26	6	18	1	0	20(24)
Sy2	7	1	25(26)	0	1	19(24)
LINER	4	0	4	0	0	9
QSO	61(63)	8	23(26)	19	2	5(8)
QSO2	8	2	31(34)	7	4	5(7)
Sbrst/HII	0(2)	0	5(12)	1	7	74(89)

Table 6. Composite spectral templates

name	Nsources	z_{min}	$\langle z \rangle$	z_{max}	λ_{min} [μm]	λ_{max} [μm]	comments
Sy1	11	0.002	0.041	0.205	5.2	24.6	Seyfert 1 with $\nu L\nu(7\mu{\rm m}) < 10^{44}$ erg s^{-1}
Sy1x	72	0.003	0.091	0.371	5.0	24.6	intermediate Seyfert types (1.2, 1.5, 1.8, 1.9)
Sy2	53	0.003	0.045	1.140	5.2	24.6	Seyfert 2 with $\nu L\nu(7\mu{\rm m}) < 10^{44}$ erg s^{-1}
LINER	16	0.001	0.034	0.322	5.2	24.6	LINER with $\nu L\nu(7\mu{\rm m}) < 10^{44}$ erg s^{-1}
QSO	125	0.020	1.092	3.355	2.5	24.6	QSO1 and Seyfert 1 with $\nu L\nu(7\mu{\rm m}) > 10^{44}$ erg s^{-1}
QSO2	65	0.031	1.062	3.700	3.6	24.6	QSO2 and Seyfert 2 with $\nu L\nu(7\mu{\rm m}) > 10^{44}$ erg s^{-1}
Sbrst	16	0.001	0.091	1.316	5.2	24.6	Starburst or HII with $\nu L\nu(7\mu{\rm m}) < 10^{44}$ erg s^{-1}
ULIRG	184	0.018	0.730	2.704	4.5	24.6	ULIRG (low and high redshift sources)
SMG	51	0.557	1.869	3.350	4.8	12.0	Submillimiter Galaxies
MIR_AGN1	119	0.002	0.455	2.190	4.0	24.6	MIR selected AGN with silicate emission
MIR_AGN2	160	0.002	0.549	2.470	4.5	24.6	MIR selected AGN with silicate absorption
MIR_SB	257	0.001	0.413	2.000	4.6	24.6	MIR selected starbursts